# **Ceramics International**

# Photocatalytic, Electrical, and magnetic properties of Carbon dots/hexaferrite's composites --Manuscript Draft--

Manuscript Number:	CERI-D-23-05387R2				
Article Type:	Full length article				
Keywords:	Hexaferrites; Photocatalysis; magnetic properties; carbon dots; composite				
Corresponding Author:	Mehar Un Nisa				
	PAKISTAN				
First Author:	Kamran Khan				
Order of Authors:	Kamran Khan				
	Karam Jabbour				
	Zahida Batool				
	Mehar Un Nisa				
	Khaled Fahmi Fawy				
	Pablo Hernandez Gomez				
	Muhammad Naeem Ashiq				
Abstract:	The Y-type hexaferrite and its nanocomposite with carbon dots have been made by using a hydrothermal approach, whereas BaSrZn2-xMnxFe12-2ySiyNiyO22 (x = 0.0, 0.25, 0.5, 0.75, and 1.0) was made using a conventional microemulsion process. A variety of approaches are used to explore the structural features, surface area, and morphology of the materials. As indicated by on-site substitutions and super-exchange interaction, saturation magnetization (Ms) and magnetic remanence (Mr) rise from 18-6 to 47.4 emu g-1 and 6.7 to 18.3 emu g-1, respectively with x,y = 0.75, although coercivity (Hc) declines from 1.4 to 0.39 kOe. The ferrite material's electrical resistivity enhanced from 25.85×106 to 49.13×106 ohm-cm. The increased saturation magnetization (Ms), magnetic remanence (Mr), and electrical resistance of ferrite material make it suitable for both high-density recording and microwave devices. The photocatalyst (composite) for the degradation of Rhodamine B in the presence of visible light was made from SrBaZn1.25Mn0.75Fe10.5Si0.75Ni0.75O22/CDs with different ratios. Photocatalysts with a modest CDs concentration (2.5wt%) successfully degraded Rhodamine B (RhB) up to 94%. After eight rounds, the composite showed excellent structural stability and good reusability. The trapping experiments confirmed that OH radical species are the major contributor in the degradation process. The composite material could be used to catch visible light and purify the environment from various pollutants in the future.				

Photocatalytic, Electrical, and magnetic properties of Carbon dots/hexaferrite's composites

Kamran Khan<sup>a</sup>, Karam Jabbour<sup>b</sup>, Zahida Batool<sup>a</sup>. Maher Un Nisa<sup>c</sup>, Khaled Fahmi Fawy<sup>d</sup>, Pablo Hernandez Gomez<sup>e</sup>, Muhammad Naeem Ashiq<sup>c</sup>,\*

<sup>a</sup> Institute of Physics, The Islamia University of Bahawalpur, Pakistan

<sup>b</sup> College of Engineering and Technology, American University of the Middle East, Egaila-54200,

Kuwait

<sup>c</sup> Institute of Chemical Sciences, Bahauddin Zakariya University, Multan-60800, Pakistan

<sup>d</sup> Department of Chemistry, Faculty of Science, King Khalid University, P.O. Box 9004, Abha 61413, Saudi Arabia.

e Departmento de Eletricidad y Electronica, Unversidad de Valladolid, Valladolid, Spain

\* = Corresponding Author

E-mail: meharuukhan786@student.bzu.edu.pk

Tell Phone No. +92-300-9879344

#### **Abstract**

The Y-type hexaferrite and its nanocomposite with carbon dots have been made by using a hydrothermal approach, whereas  $BaSrZn_{2-x}Mn_xFe_{12-2v}Si_vNi_vO_{22}$  (x = 0.0, 0.25, 0.5, 0.75, and 1.0) was made using a conventional microemulsion process. A variety of approaches are used to explore the structural features, surface area, and morphology of the materials. As indicated by onsite substitutions and super-exchange interaction, saturation magnetization (Ms) and magnetic remanence (Mr) rise from 18-6 to 47.4 emu g<sup>-1</sup> and 6.7 to 18.3 emu g<sup>-1</sup>, respectively with x,y = 0.75, although coercivity (Hc) declines from 1.4 to 0.39 kOe. The ferrite material's electrical resistivity enhanced from 25.85×10<sup>6</sup> to 49.13×10<sup>6</sup> ohm-cm. The increased saturation magnetization (Ms), magnetic remanence (Mr), and electrical resistance of ferrite material make it suitable for both high-density recording and microwave devices. The photocatalyst (composite) for the degradation of Rhodamine B in the presence of visible light was made from SrBaZn<sub>1.25</sub>Mn<sub>0.75</sub>Fe<sub>10.5</sub>Si<sub>0.75</sub>Ni<sub>0.75</sub>O<sub>22</sub>/CDs with different ratios. Photocatalysts with a modest CDs concentration (2.5wt%) successfully degraded Rhodamine B (RhB) up to 94%. After eight rounds, the composite showed excellent structural stability and good reusability. The trapping experiments confirmed that OH radical species are the major contributor in the degradation process. The composite material could be used to catch visible light and purify the environment from various pollutants in the future.

Keywords: Hexaferrites; Photocatalysis; Magnetic properties; Carbon dots; composite

#### 1. Introduction

Nanomaterials are currently known as a fresh and intriguing category of materials owing to their unique features. They offer remarkable electrical, mechanical, magnetic, thermal, and optical properties because of their specific surface energy, enhanced surface area, and dense size [1–6] The structural properties of nanoparticles have allowed them to expand their range of applications. Ferrites materials have excellent electrochemical, electrical, dielectric, catalytic, and magnetic properties. Ferrites could be employed in electrical and microwave devices, as well as photocatalysts for the degradation of various pollutants due to their narrow band gap. Based on magnetism, ferrites are classified as either soft or hard materials, and ferrites are categorized as spinel, garnet, or hexagonal depending on their crystalline structure [7–9]. Further, the hexaferrite are classified based on their composition having six types: M-type (BaFe<sub>12</sub>O<sub>19</sub>) [10], U-type (Ba<sub>4</sub>Me<sub>2</sub>Fe<sub>36</sub>O<sub>60</sub>)[11], X-type (Ba<sub>2</sub>Me<sub>2</sub>Fe<sub>28</sub>O<sub>46</sub>)[12], W-type (BaMe<sub>2</sub>Fe<sub>16</sub>O<sub>27</sub>)[13], Y-type (Ba<sub>2</sub>Me<sub>2</sub>Fe<sub>12</sub>O<sub>22</sub>) [14], and Z-type (Ba<sub>3</sub>Me<sub>2</sub>Fe<sub>24</sub>O<sub>41</sub>) [15].

As a result of rapid industry expansion, water pollution has become a major problem around the world, and the majority of industries, including paper, textiles, food, printing, medicines, and cosmetics, use dyes to improve product quality[16]. All of these enterprises generate large amounts of colored effluent, which is discharged into the adjacent lakes, rivers, and other bodies of water. Because these pigments are non-biodegradable, cancerous, and mutagenic, they are dangerous to humans and marine life equally [17,18]. The radish violet dye rhodamine B is extensively utilized in fabric and foodstuff. This pigment is toxic to the eyes, scalp, and cardiovascular system, and is carcinogenic, neurotoxic, and reproductively damaging in animal tests. As a result, removing this dye from wastewater is crucial for human and marine life protection [19,20].

To remove the coloring ingredient from wastewater [21], adsorption [22], photochemical degradation [23], superior oxidation [24], and coagulation [25] have all been utilized. Out of the most environmentally friendly and clean methods of eliminating dyes from wastewater is photocatalytic degradation. Various oxide semiconductor photocatalysts have been used for this purpose, including Zinc oxide (ZnO) [26], Nickel oxide (NiO) [27], Copper oxide (CuO) [28], Fe<sub>2</sub>O<sub>3</sub>[29], Bi<sub>2</sub>WO<sub>6</sub> [30], and reduced graphene oxide-Fe<sub>3</sub>O<sub>4</sub>/TiO<sub>2</sub> [31]. Because of their improved chemistry and photo-corrosion durability, magnetic oxide materials with spinel structure having general formula MFe<sub>2</sub>O<sub>4</sub> (as M = divalent cation like Mn<sup>2+</sup>, Ni<sup>2+</sup>, Mg<sup>2+</sup>, Cu<sup>2+</sup>, Co<sup>2+</sup>, etc.) are gaining popularity as photocatalysts [32]. To boost the photocatalytic efficacy of these materials, several researchers doped, replaced, and formed composites with other materials. Hexaferrites, especially Y-type hexaferrites, outperform spinel ferrites in terms of magnetic properties, superior chemical and thermal stability, stronger electrical resistivity for microwave applications, and improved corrosion resistance [33]. The substituted Y-type hexaferrite was used in conjunction with the carbon dots in this study since Y-type hexaferrite has been underutilized in the photocatalytic degradation procedure of industrially important dye. Broad-spectrum sunlight absorbance, chemical stability, nontoxicity, photosensitization, rapid bioactivity, and a range of simple production techniques are among the chemical and photophysical features of carbon dots (CDs) [34-37]. Because of their characteristics, carbon dots were employed to make composites with Y-type hexaferrite material. Carbon dots with a smaller band gap absorb more light and prevent photogenerated electron/hole pairs from recombination, hence increasing the efficiency of the composite material [38].

Due to the low dc electrical resistivity of the spinel ferrites as compared to hexaferrite, they can not be used at high frequency i.e. gigahertz and the Y-type hexaferrites are the best choice for this

purpose. The morphology and the particle size of the ferrites materials are greatly affected by the method used for their synthesis. Various methods have been reported for the synthesis of Y-type hexaferrites such as solid state reaction method, coprecipitation, sol-gel, hydrothermal and microemulsion method. The solid state reaction method required very high temperature and one can not get the uniform distribution of the particles and good morphology. The coprecipitation and sol-gel methods also have little control on the morphology while the microemaulsion method can control the particle size as well as the morphology by using surfactants which act nano-reactors by forming the micelles. Therefore, in this study the microemulsion method has been used for the fabrication of all Y-type hexaferrite materials [39–41]

The morphological and electromagnetic characteristics of Y and M-type hexaferrite have been altered in recent years using trivalent or divalent ions, as well as their dual metal cation interaction as dopants or substituents at iron as well as other divalent metal ions. As a result, numerous ions have been replaced at the iron and divalent cation sites, such as Al-Ga [42], Al-In [43], La-Mn [44], Ce-Ni[45], Bi-Cr [46], Ti-Co [47], Fe[48], Ni-Mg [49], Al [50], In [51], and combinations of tetravalent as well as divalent ions, like Ni–Zr, Cu-Zr, Zn-Zr, Ni-Ti, Mn-Zr, Co-Ti [52]. As a result of substitution, only a few situations have improved both electric and magnetic features. The primary purpose of the research was to optimize the properties of electricity and magnetism at the same time as the substituted material so that it could be used at high frequencies and high-density recording media.

The SrBaZn<sub>1.25</sub>Mn<sub>0.75</sub>Fe<sub>10.5</sub>Si<sub>0.75</sub>Ni<sub>0.75</sub>O<sub>22</sub>/CDs nanocomposite is a novel photocatalyst material with highly promising electrical, magnetic and photocatalytic characteristics. Unlike typical photocatalysts, this material combines the synergistic effects of various metal in the ferrite with

carbon dots (CDs). In this case, CDs inclusion not only boosts the photocatalytic performance but also brings exceptional light absorption and charge separation capabilities. Furthermore, the precisely tailored composition and structure of SrBaZn<sub>1.25</sub>Mn<sub>0.75</sub>Fe<sub>10.5</sub>Si<sub>0.75</sub>Ni<sub>0.75</sub>O<sub>22</sub>/CDs result in improved stability, lower recombination losses, and longer material longevity. This innovation has significant promise for numerous environmental remediation procedures, water purification, and solar-powered energy conversion, making it a ground breaking and promising photocatalytic material.

The structural, electrical, and magnetic properties of  $SrBaZn_{1-x}Mn_xFe_{12-2y}Si_yNi_yO_{22}$  (x, y = 0.0, 0.25, 0.5, 0.75, and 1) Y-type hexaferrites were investigated.  $SrBaZn_{1.25}Mn_{0.75}Fe_{10.5}Si_{0.75}Ni_{0.75}O_{22}$  outperformed all other materials in terms of electrical and magnetic properties, hence it was chosen for the manufacturing of carbon dot composites (CDs). The photocatalytic activity of the 1:0.25 composite ( $SrBaZn_{1.25}Mn_{0.75}Fe_{10.5}Si_{0.75}Ni_{0.75}O_{22}$ : CDs) was found to be higher than that of other composite materials, and the photocatalytic method was examined.

# 2. Experimental

#### 2.1. Chemical used

The chemicals used for the fabrication of all the materials were iron nitrate (Fe(NO<sub>3</sub>)<sub>3</sub>.9H<sub>2</sub>O, Sigma-Aldrich, 98%), strontium nitrate (Sr(NO<sub>3</sub>)<sub>2</sub>, Sigma-Aldrich, 99.8%), barium nitrate (Ba(NO<sub>3</sub>)<sub>2</sub>, Merck, 99.0%), nickel nitrate (Ni(NO<sub>3</sub>)<sub>2</sub>. 6H<sub>2</sub>O, Sigma-Aldrich, 99.6%), zinc nitrate (Zn(NO<sub>3</sub>)<sub>2</sub>, 6H<sub>2</sub>O, Sigma-Aldrich, 98%), manganese acetate (Mn(CH<sub>3</sub>COO)<sub>2</sub>, Sigma-Aldrich, 98%), cetyltriammonium bromide (CTAB, C<sub>16</sub>H<sub>33</sub>N(CH<sub>3</sub>)<sub>3</sub>Br, Sigma-Aldrich, 98%), silicon tetrachloride (SiCl<sub>4</sub>, Sigma-Aldrich, 99%) and milk (commercial grade, Nestle). The deionized water was used for the preparation of the solutions.

# 2.2. Y-type hexaferrite fabrication

With x,y values of 0.0, 0.25, 0.5, 0.75, and 1.0, the Y-type hexaferrite SrBaZn<sub>2-x</sub>Mn<sub>x</sub>Fe<sub>12-2y</sub>Si<sub>y</sub>Ni<sub>y</sub>O<sub>22</sub> was synthesized via a simple micro-emulsion technique. The solutions of metal nitrates such as Fe(NO<sub>3</sub>)<sub>3</sub>.9H<sub>2</sub>O (0.1 M), Sr(NO<sub>3</sub>)<sub>2</sub> and Ba(NO<sub>3</sub>)<sub>2</sub> (0.0083 M), and zinc nitrate hexahydrate (0.017 M) were prepared in deionized water and substituent (Mn, Si and Ni) concentrations were changed as appropriate using their metal salts. On a magnetic hot plate, all of these solutions were agitated, and CTAB was added as a surfactant in a metal: CTAB ratio (1:1.5). The pH of each mixed solution was maintained at 11–12 to produce precipitates by gradually adding 2.0 M KOH liquid dropwise. The mixture was shaken for a further two hours to get homogeneous particles. Following centrifugation, the precipitates were obtained and washed many times using DI water till the pH of the mixture was reduced to 7. The product was allowed to dry in an oven at 90 °C before being annealed for nine hours at 1000 °C in a muffle furnace to obtain the final required product.

# 2.3 Preparation of Carbon dots

Using a hydrothermal process, carbon dots (CDs) were created by combining 48 mL of water and 60 mL of milk. After that, the liquid was vigorously agitated for 20 minutes over a hot plate with magnetic stirrer. The mixture of milk and water was then placed into a 100 mL autoclave, which was then filled to 80 percent of its capability. The filled autoclave was inserted at 180 °C in an electrical oven for 2 hours before being allowed to cool gradually to ambient temperature. The material was extracted, washed, and rinsed numerous times with DI water. The substance was finally dried at 100 °C and kept in a desiccator for subsequent analysis.

# 2.4 Composite Fabrication

The hexaferrite with composition (BaSrZn<sub>1.25</sub>Mn<sub>0.75</sub>Fe<sub>10.5</sub>Si<sub>0.75</sub>Ni<sub>0.75</sub>O<sub>22</sub>) and carbon dots composites with various ratios 1:0, 1:0.25, 1:0.5, and 1:0.75 were fabricated via hydrothermal route. The milk (60 mL) was mixed with 48 mL of water and also added already synthesized hexaferrite having specific composition of BaSrZn<sub>1.25</sub>Mn<sub>0.75</sub>Fe<sub>10.5</sub>Si<sub>0.75</sub>Ni<sub>0.75</sub>O<sub>22</sub> with different amounts related to various ratios. The milk/water and hexaferrite combination was stirred for about 2 hours. The entire mixture was therefore placed in an autoclave and placed for two hours at 180 °C for two hours. The rest of the procedure was the same as mentioned in section 2.3.

# 2.5 Catalyst characterization

The structure of the synthesized materials was confirmed using a Rigaku D/max-Ultima X-ray analyzer. The material's surface area was determined utilizing BET measurement by Micrometrics 2460, and its morphology was studied through a scanning electron microscope (JSM-5600LV). A UV–vis spectrophotometer (UV759S) was used to explore the optical properties of materials. Photoluminescence (PL) spectroscopy was used to confirm the recombination between electrons and holes via a Confocal micro-Pl/Raman spectrometer. A two-point probe procedure has been used for the measurement of direct-current resistivity via a Kiethly-2400 source meter, and magnetic properties were obtained with a vibrating sample magnetometer (VSM lakeshore-7900).

# 2.6. Photocatalytic experiments

Degrading Rhodamine B (RhB) dye in an aqueous medium was used to examine the photocatalytic properties of the manufactured photocatalysts. As a source of light, a 350 W Xe lamp with a minimum filtration system at 420 nm was used. A 100.00 mL (20 ppm) RhB solution and a 10.0 mg L<sup>-1</sup> photocatalytic material were mixed. To establish adsorption/desorption equilibrium, this mixture was stirred in the darkness for 30 minutes. The catalytic substance was centrifuged from 5.00 mL samples that were collected after every 20 minutes. With the use of a UV-vis

spectrophotometer, the Beer-Lambert law was used to calculate the proportion of RhB present in the samples (UV759S). Control studies were carried out to demonstrate that the presence of a photo-catalyst and radiation cause dye degradation. As a result, the reaction mixture was held in light in the initial investigation alone without the inclusion of a photocatalyst, whereas the photocatalyst was introduced to the dyes in the darkness during the second experiment. In both cases, the absorbance varies very little, showing that the degradation of the dye is due to the presence of light and photocatalyst (photocatalytic process). The little reduction in absorbance may be due to the adsorption process on the surface of the photocatalyst which was corrected while calculating the photodegradation efficiency.

#### 3. Results and discussion

# 3.1 Structural and Surface Properties Investigation

The production of hexagonal phases in synthetic materials was determined by powder X-ray diffraction analysis. The XRD spectra of substituted products ( $SrBaZn_{2-x}Mn_xFe_{12-2y}Si_yNi_yO_{22}$  where  $x\&y=0.0,\ 0.25,\ 0.5,\ 0.75$  and 1.0) and composite material ( $CDs/SrBaZn_{1.25}Mn_{0.75}Fe_{10.5}Sn_{0.75}Ni_{0.75}O_{22}$ ) are shown in Figure 1. All of the diffracted peaks completely fit the conventional pattern JCPDS No. 00-025-1193 without a single additional peak showing the distinct phase of Y-type hexagonal ferrites. The peak of the composite material, about 2-theta =  $26^{\circ}$ , corresponds to previously reported carbon dots having an hkl value (002), indicating that the composite material has been fabricated successfully.

Several properties, particularly lattice parameters (a&c, cell volume), and crystallite size (S), were calculated from the X-ray diffraction patterns by using formulas [53]. The effect of chemical content on lattice parameters (a and c) and cell volume is illustrated in Table 1.0. The increase in cell parameters with substituent contents has been described by ionic radii of the substituents i.e.

Mn<sup>2+</sup> (0.80 Å) and Ni<sup>2+</sup> (0.72 Å) have greater ionic radii than metal ions Zn<sup>2+</sup> (0.74 Å) and Fe<sup>3+</sup> (0.64 Å). The similar types of result are reported in the literature i.e. if the substituents ionic radius is greater than the host then it will increase the lattice parameters and vice versa [37,50,51]. According to the Scherer formula, the crystal size of the generated materials ranges between 50 and 87 nm depending on peak broadening in the XRD analysis. The crystallite size is in agreement with that of the already reported ferrites materials [36,37,52,54]. The lattice parameters of the present work has also been compared with that of the substituted Y-type hexaferrites reported in the literature as shown in supplementary materials (table S1). The reduced crystallite size of the nanocomposites enables a greater surface area, which is advantageous for catalytic processes.

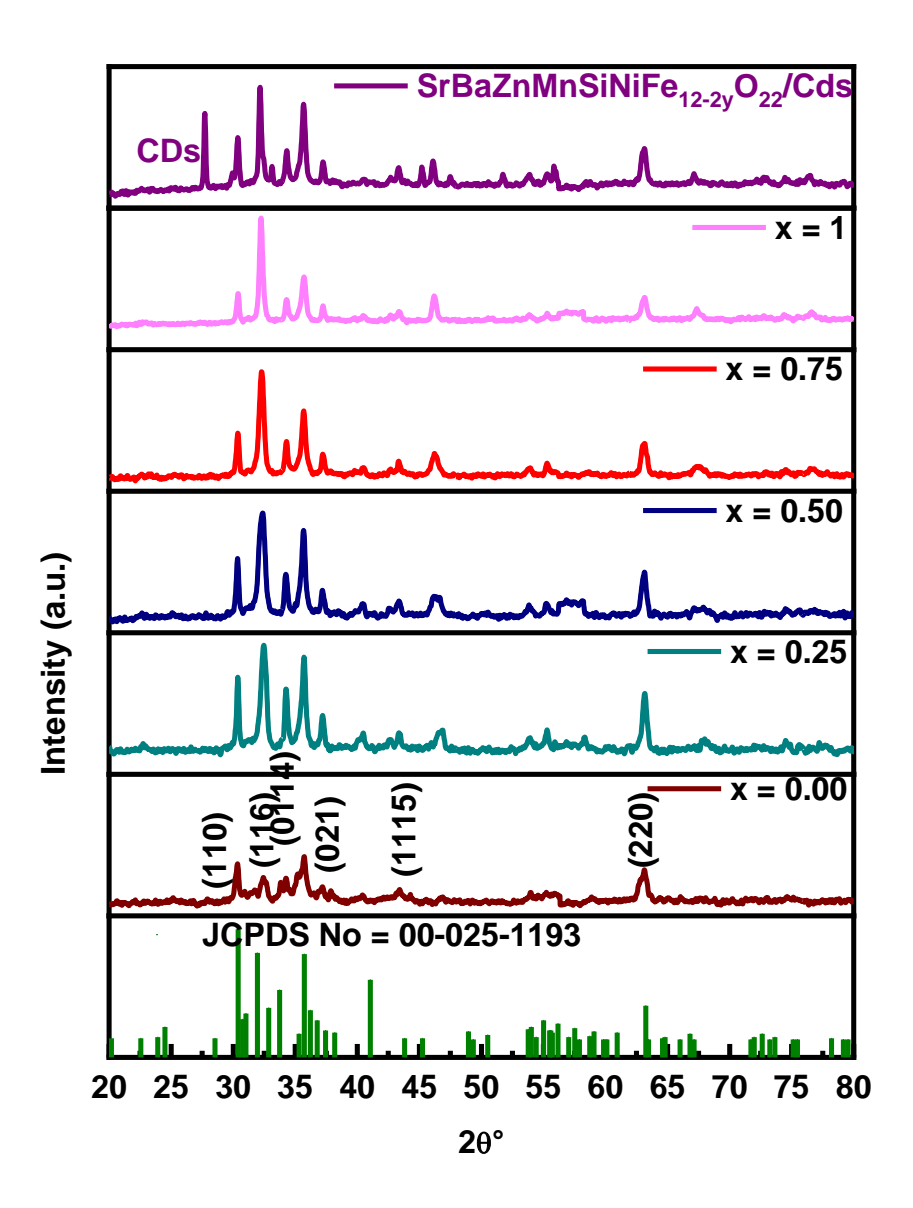


**Figure 1:** X-ray diffraction patterns for  $SrBaZn_{1-x}Mn_xFe_{12-2y}Si_yNi_yO_{22}$  (x, y = 0.0, 0.25, 0.5, 0.75 and 1.0) and the composite (CDs/SrBaZn<sub>1.25</sub>Mn<sub>0.75</sub>Fe<sub>10.5</sub>Si<sub>0.75</sub>Ni<sub>0.75</sub>O<sub>22</sub> with ratio 0.25/1.0).

**Table 1.0:** Cell constants, volume (a & c, Vcell), crystallite size (S), and magnetic parameters for  $SrBaZn_{2-x}Mn_xFe_{12-2y}Si_yNi_yO_{22}$ .

Substituents	a	c (Å)	Cell	Crystallite	Saturation	Remanence	Coercivity
contents	$(\mathring{\mathbf{A}})$		volume	size (nm)	magnetic.	(emu g <sup>-1</sup> )	(KOe)
			$(\mathring{\mathbf{A}}^3)$		(emu g <sup>-1</sup> )		
x.y = 0	5.81	43.01	1257.3	56	18.6	6.7	1.40
x,y = 0.25	5.82	43.03	1262.2	62	17.8	7.1	0.51
x,y = 0.5	5.84	43.04	1271.2	87	44.2	15.0	1.05
x,y = 0.75	5.85	43.07	1276.5	69	47.7	18.3	0.40
x,y = 1.0	5.86	43.09	1281.4	57	27.0	8.4	0.39
Composite				52	33.4	10.6	0.43

The particle morphology and crystallite size of the generated composites were examined using SEM methods, and the results are displayed in Figures 2a-d. Figures 2a&b show SrBaZn<sub>2</sub>Fe<sub>12</sub>O<sub>22</sub> and SrBaZn<sub>1.25</sub>Mn<sub>0.75</sub>Fe<sub>10.5</sub>Si<sub>0.75</sub>Ni<sub>0.75</sub>O<sub>22</sub>, respectively and particles are spherical. Some of the particles are agglomerated due to the magnetic nature of ferrites particles. The grain size calculated by Image j is in the 150 to 200 nm range which is in agreement with that calculated from XRD data. In the case of carbon dots (figure 2c), thin sheet type morphology appeared whilst small ferrite particles have been ornamented on the exterior of carbon dots (figure 2d) in the composite

while the thin sheets of carbon dots are arranged like flower's petals. The size of particles in a material can commonly exceed the size of crystallites due to the presence of flaws and faults at grain boundaries. Crystallites are ordered atomic arrangements within a substance that form during the crystallization process during solidification or recrystallization. Although these crystallites have a well-defined atomic structure, they are not perfect; dislocations, vacancies, and grain boundaries can exist at their edges (Lu, 2000). In contrast, particles are aggregates of crystallites or non-crystalline substances. When a material is mechanically processed or recrystallized, new grains with different orientations can nucleate and develop, resulting in a variety of grain sizes. The existence of tiny crystallites or even amorphous regions within particles adds to their larger size when compared to individual crystallite sizes (Gleiter, 1989). The surface area of carbon dots (CDs), ferrite (SrBaZn<sub>1.25</sub>Mn<sub>0.75</sub>Fe<sub>10.5</sub>Si<sub>0.75</sub>Ni<sub>0.75</sub>O<sub>22</sub>), and composite were evaluated using BET investigation and N2 sorption isotherm models are shown in Figure 3. The surface area of the composite (186.0 m<sup>2</sup> g<sup>-1</sup>) is much larger than the surface area of the pristine materials i.e.  $SrBaZn_{1.25}Mn_{0.75}Fe_{10.5}Si_{0.75}Ni_{0.75}O_{22}$  (83.0 m<sup>2</sup> g<sup>-1</sup>) and carbon dots (133.0 m<sup>2</sup> g<sup>-1</sup>). The larger the surface area, the more active sites it will have on its surface, which is a need for employing it as a photocatalyst.

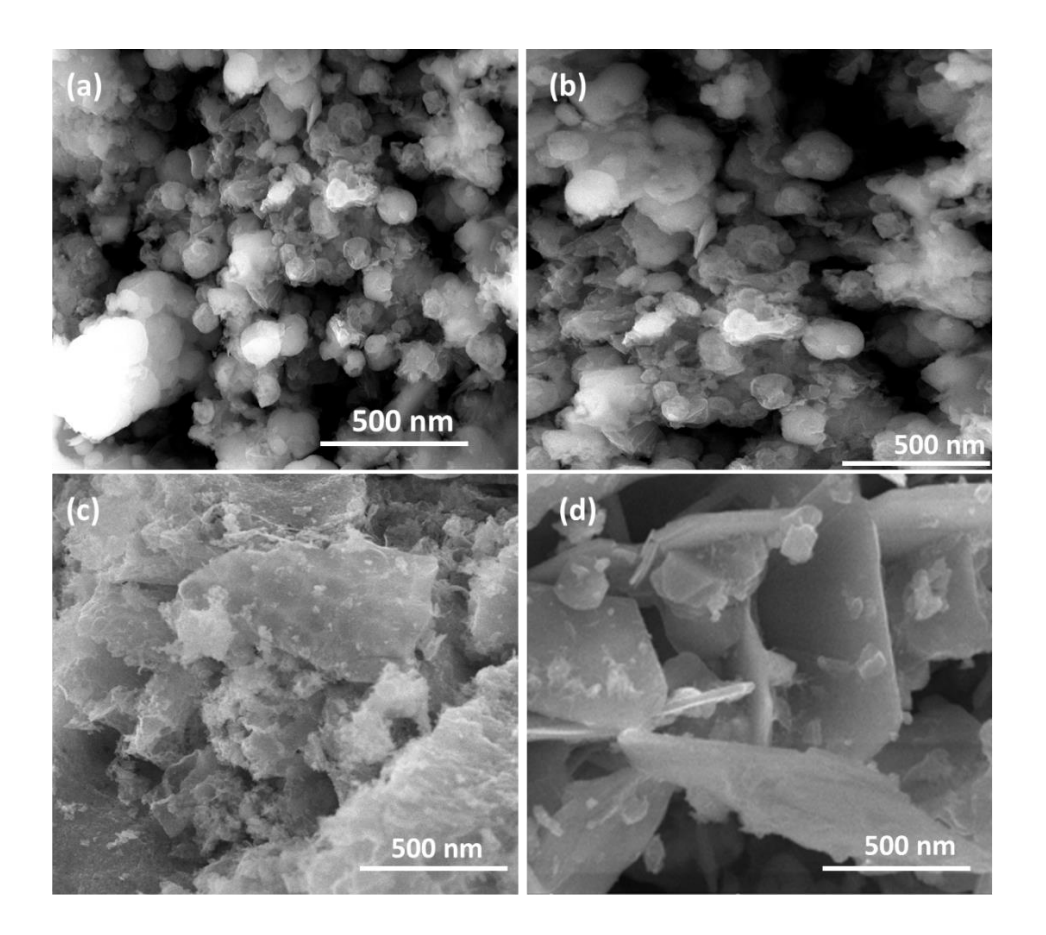


**Figure 2:** SEM images for (a)  $SrBaZn_2Fe_{12}O_{22}$ , (b)  $SrBaZn_{1.5}Mn_{0.5}Fe_{11}Sn_{0.5}Ni_{0.5}O_{22}$ , (c) carbon dots and (d)  $CDs/SrBaZn_{1.5}Mn_{0.5}Fe_{11}Sn_{0.5}Ni_{0.5}O_{22}$  composite

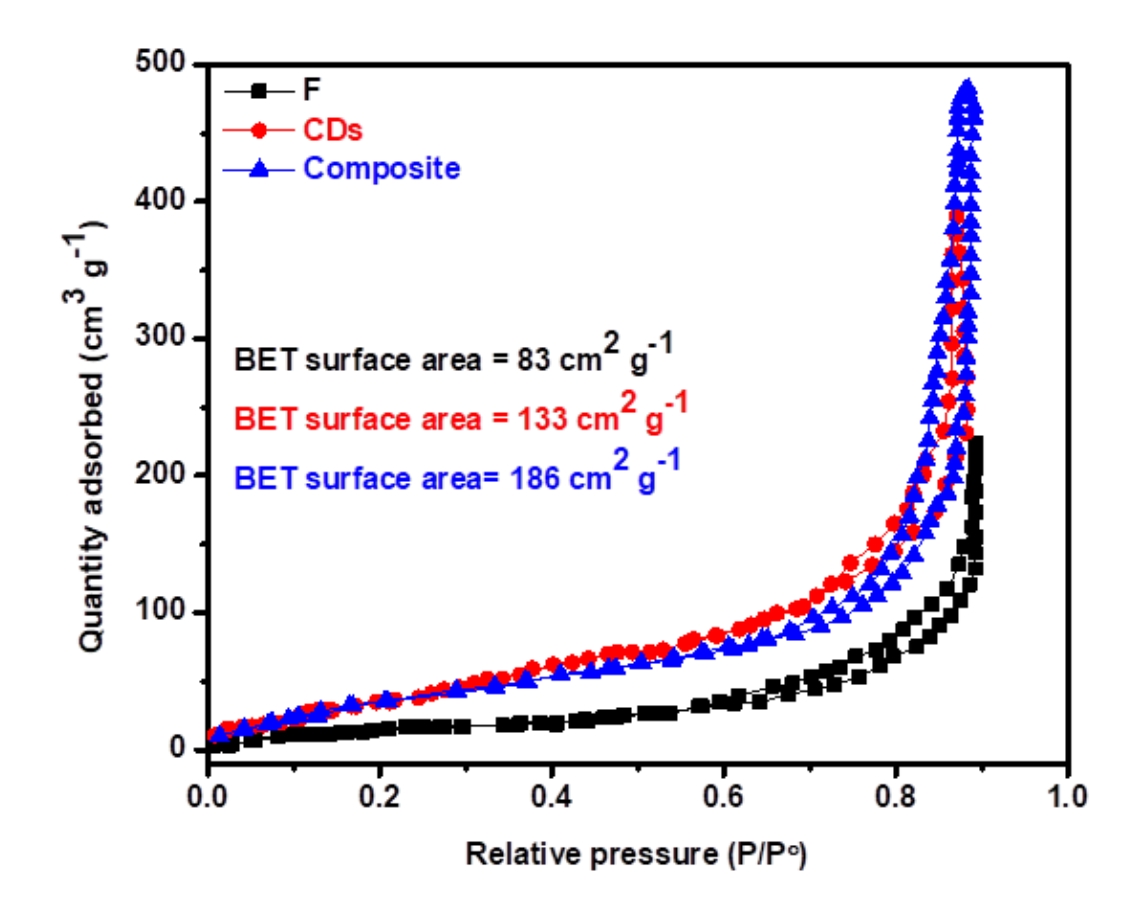


**Figure 3:** BET isotherms for  $SrBaZn_{1.25}Mn_{0.75}Fe_{10.5}Si_{0.75}Ni_{0.75}O_{22}$ , carbon dots and  $CDs/SrBaZn_{1.25}Mn_{0.75}Fe_{10.5}Si_{0.75}Ni_{0.75}O_{22}$  composite

# 3.3 Magnetic and electrical properties

The two-point probe approach was used to evaluate the fluctuation in dc electrical resistivity with substituent content of generated materials as given in Figure 4. The ferrites material's resistivity climbs from  $25.85 \times 10^6$  to  $49.13 \times 10^6$   $\Omega$  cm as the dopant amount increases, the optimum value was obtained at x,y=0.75, and then began to fall. The conduction mechanism in Y-type hexaferrites is the transfer of electrons from Fe<sup>3+</sup> to Fe<sup>2+</sup> ions at the octahedral site [55]. When Ni<sup>2+</sup> substituted Fe<sup>3+</sup> at the octahedral region, the total amount of ferric ions at the octahedral site reduced, as did electron hopping and, as a result, conductivity also decreased.

The substitution will also produce the holes to compensate for the charges, the conduction mechanism is provided this time by electron hopping among the ferric and ferrous states as well as by the hopping of holes but because holes are more difficult to hop than electrons, the material's resistance rises. When silicon ions replace iron ions at the tetrahedral site, the Si(IV) ions push part of the iron ions to the octahedral position, resulting in an increase in ferric ions concentration at that site and consequently, the conductivity increased. This impact is modest at lower doses and does not influence resistivity. Owing to the improved conductivity of the carbon dots, the composite material's resistivity is lower than that of SrBaZn<sub>1.25</sub>Mn<sub>0.75</sub>Fe<sub>10.5</sub>Si<sub>0.75</sub>Ni<sub>0.75</sub>O<sub>22</sub>. Carbon dots with C-C sp2 hybridization allow electrons from neighboring carbon atoms and ferrite surface regions to overlap, improving the conductivity of composite materials. The higher the ferrite material's resistivity, the more likely it is to be employed in microwave devices, which demand extremely high resistive materials [45]. SrBaZn<sub>1.25</sub>Mn<sub>0.75</sub>Fe<sub>10.5</sub>Si<sub>0.75</sub>Ni<sub>0.75</sub>O<sub>22</sub> has a higher resistivity than all other fabricated materials indicating that it can be utilized in microwave devices.

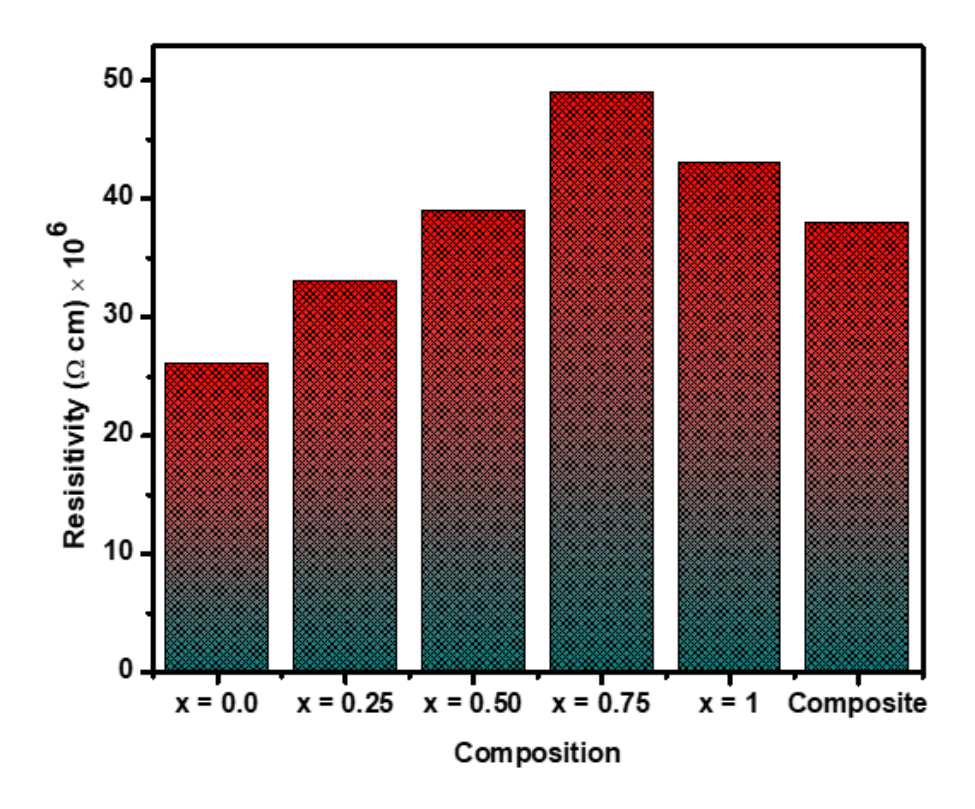


**Figure 4:** Relationship between composition and DC electrical resistivity of all the fabricated materials.

Using the hysteresis loops shown in Figure 5, magnetic characteristics like coercivity (Hc), saturation magnetization (Ms), and remanence (Mr) were calculated. As demonstrated in Table 1.0, the Ms, Mr, and Hc values rise until x, y = 0.75, then fall as the substituent level rises. The development of the cation distribution at various sub-lattice positions can be linked to the change in these magnetic characteristics. Each unit cell of the Y-type hexaferrite structure, which is built up of 3TS blocks with the general formulas  $S = Me_2^{2+}Fe_4^{3+}O_8$  and  $T = Ba_2^{2+}Fe_8^{3+}O_{14}$ , is made up of three formula units. The cations are clustered at each sub-lattice location as follows:  $6c_{IV}$  (tetrahedral, 2),  $3a_{VI}$  (octahedral, 1),  $6c_{VI}$  (octahedral, 2),  $18h_{VI}$  (Octahedral, 6),  $6c_{IV}$  (tetrahedral, 2),  $3b_{VI}$  (octahedral, 1). The electrons at three different sites (3av1, 18hVI, and 3b1) spin in an upward direction, whereas the downward spin at the other sites. The cation  $Si^{4+}$  appears to have tetrahedral site preferences, whereas  $Ni^{2+}$  appears to have octahedral preferences.  $Si^{4+}$  has no unpaired

electrons in its outermost shell, whereas  $Ni^{2+}$  has three unpaired electrons which indicates that the silicon ion has 0 Bohar magneton magnetic moment while nickel ion has three. When non-magnetic silicon (IV) replaced ferric ions (which had 5 unpaired electrons i.e. magnetic moment of 5 Bohar magneton) from the tetrahedral position in which the electrons have downward spin, therefore, the number of unpaired electrons at the octahedral site have upward spin will be increased. Even though Ni(II) replaces ferric at the octahedral site, after accounting for opposing spins, the overall quantity of unpaired e's grows in the upward direction, resulting in higher saturation magnetization and remanence. Another reason for the increase in both the Ms and Mr. is indeed the substitution of Mn2+, which has five unpaired electrons, for  $Zn^{2+}$ , which has no unpaired electrons. Mr and Ms parameters of the  $SrBaZn_{1.25}Mn_{0.75}Fe_{10.55}Si_{0.75}Ni_{0.75}O_{22}$  /CDs composite material were lower than those of the ferrite material (ratio 1:0.25). The drop in magnetic parameters could be due to the non-magnetic nature of the carbon dots. After x, y = 0.75, both values drop as a result of a reduction in super-exchange connections brought on by non-magnetic Si(IV) ions [55–57].

As shown in Table 1, the coercivity (Hc) of the generated materials decreases as the replacement level rises. The decrease in the value of coercivity can be explained by the equation,  $Hc = K1/\mu_0Ms$ . The evidence supports the following rule: when Ms rises, Hc falls, and vice versa.  $SrBaZn_{1.25}Mn_{0.75}Fe_{10.5}Si_{0.75}Ni_{0.75}O_{22}$  is the optimum material for use in high-density recording medium, as indicated by increases in Ms and Mr and decreases in Hc values. As a result,  $SrBaZn_{1.25}Mn_{0.75}Fe_{10.5}Si_{0.75}Ni_{0.75}O_{22}$  was chosen for the production of carbon dot composites for photocatalytic applications. The comparison of all the magnetic parameters with the already reported materials has been given in supplementary materials (Table S2) showing that the present material showed better magnetic properties.

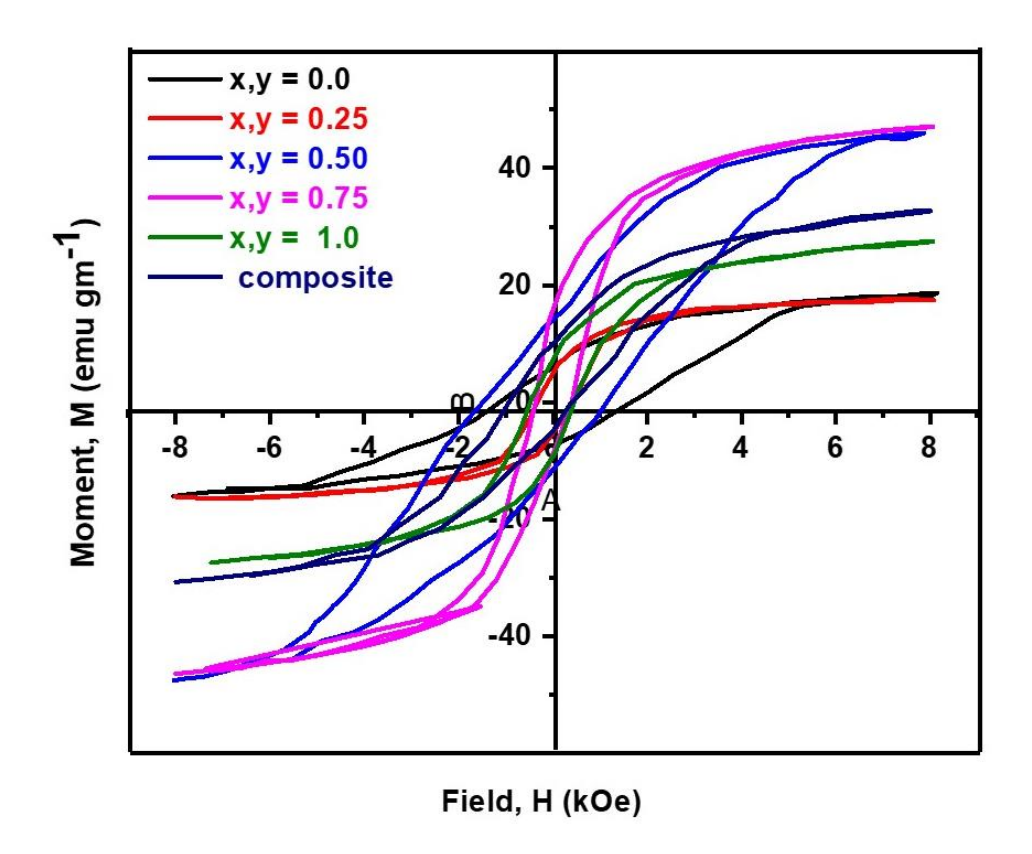


**Figure 5:** M-H loops for  $SrBaZn_{1-x}Mn_xFe_{12-2y}Si_yNi_yO_{22}$  (x, y = 0.0, 0.25, 0.5, 0.75 and 1.0) and the composite (CDs/SrBaZn<sub>1.25</sub>Mn<sub>0.75</sub>Fe<sub>10.5</sub>Si<sub>0.75</sub>Ni<sub>0.75</sub>O<sub>22</sub> with ratio 0.25/1.0).

# 3.3 Optical features

Figure 6 displays the diffuse reflectance spectra and optical characteristics of photocatalysts., including substituted hexaferrite (SrBaZn<sub>1.25</sub>Mn<sub>0.75</sub>Fe<sub>10.5</sub>Si<sub>0.75</sub>Ni<sub>0.75</sub>O<sub>22</sub>), carbon dots (CDs), and composite (CDs/ SrBaZn<sub>1.25</sub>Mn<sub>0.75</sub>Fe<sub>10.5</sub>Si<sub>0.75</sub>Ni<sub>0.75</sub>O<sub>22</sub>) with a 0.25/1.0 ratio. According to the Tauc figure, the band gap for ferrite material is 2.6 eV, 2.9 eV for CDs, and 2.22 eV for composite material. The composite material's band gap is lower than that of individual components such as CDs and SrBaZn<sub>1.25</sub>Mn<sub>0.75</sub>Fe<sub>10.5</sub>Si<sub>0.75</sub>Ni<sub>0.75</sub>O<sub>22</sub>, indicating that it can absorb more visible light. The primary criterion for choosing a photocatalyst for usage in sunlight is that it comprises 45 percent of the visible range, so sunshine can be used as a light source [58,59].

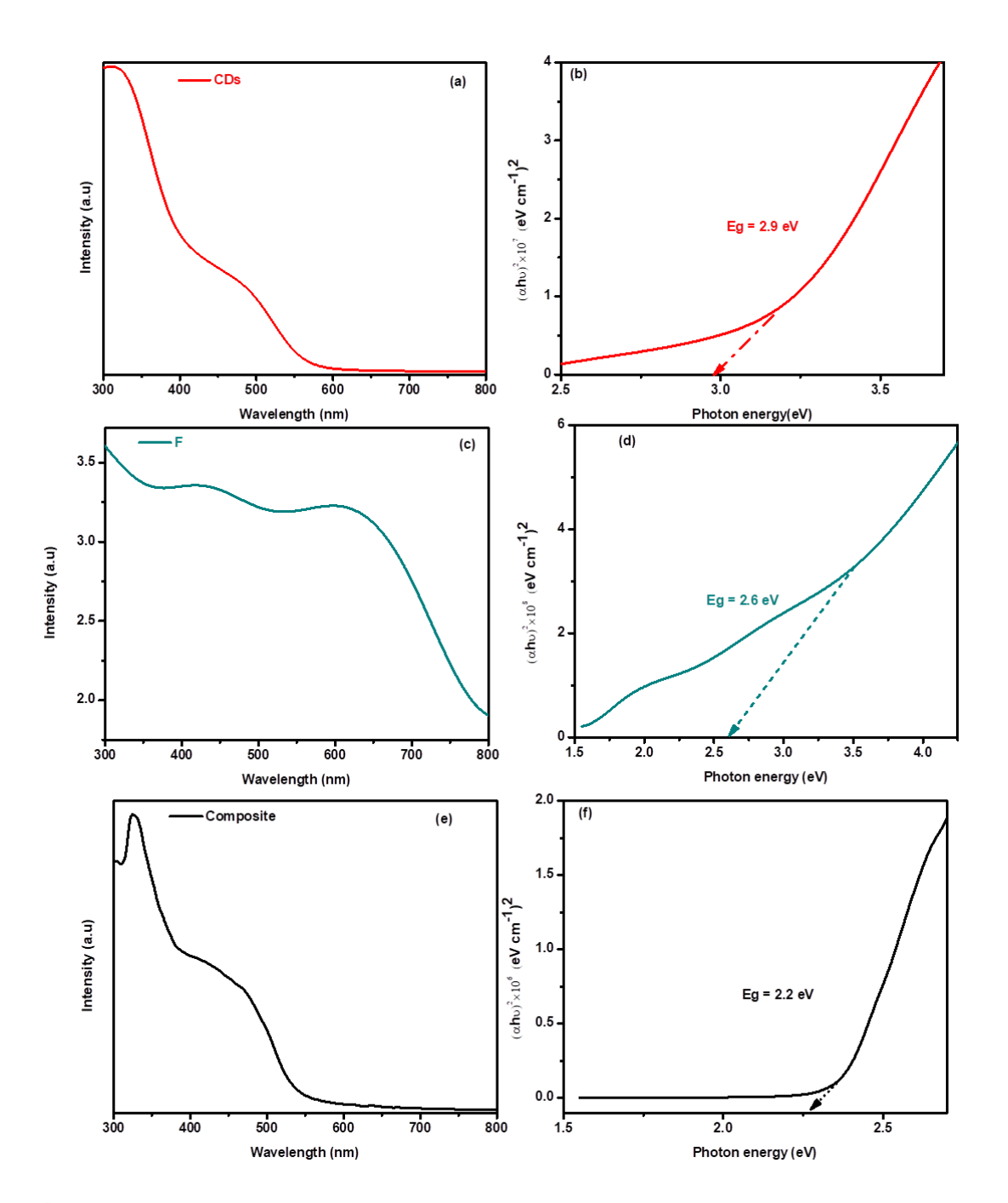


**Figure 6:** UV/vis. spectrum and Tauc graphs for CDS,  $SrBaZn_{1.25}Mn_{0.75}Fe_{10.5}Si_{0.75}Ni_{0.75}O_{22}$ , and composite (CDs/SrBaZn<sub>1.25</sub>Mn<sub>0.75</sub>Fe<sub>10.5</sub>Si<sub>0.75</sub>Ni<sub>0.75</sub>O<sub>22</sub> with ratio 0.25/1.0)

Photoluminescence (PL) investigations can be used to evaluate migration, charge carrier setup, and separation. The fluorescence intensity for the hexaferrite (SrBaZn<sub>1.25</sub>Mn<sub>0.75</sub>Fe<sub>10.5</sub>Si<sub>0.75</sub>Ni<sub>0.75</sub>O<sub>22</sub>) and CDs material was rather high, indicating a lot of

electron/hole recombination. The composite's PL spectrum displays lower peak intensity than that of the other materials, suggesting a higher possibility for electron/hole separation and a potential increase in the composite's photocatalytic effectiveness [59–61]. The presence of two peaks in the photoluminescence (PL) spectrum of materials at 409 and 462 nm can be attributed to the material's unique electronic structure and crystal lattice properties. The first peak at 409 nm likely arises from electron transitions between energy levels within the material's band structure, while the second peak at 462 nm may be associated with the presence of defects or impurities within the crystal lattice, resulting in localized electronic states. The distinct energy levels and transitions between them lead to the observed emission peaks in the PL spectrum, providing valuable insights into the material's optoelectronic properties and its potential applications in diverse fields.

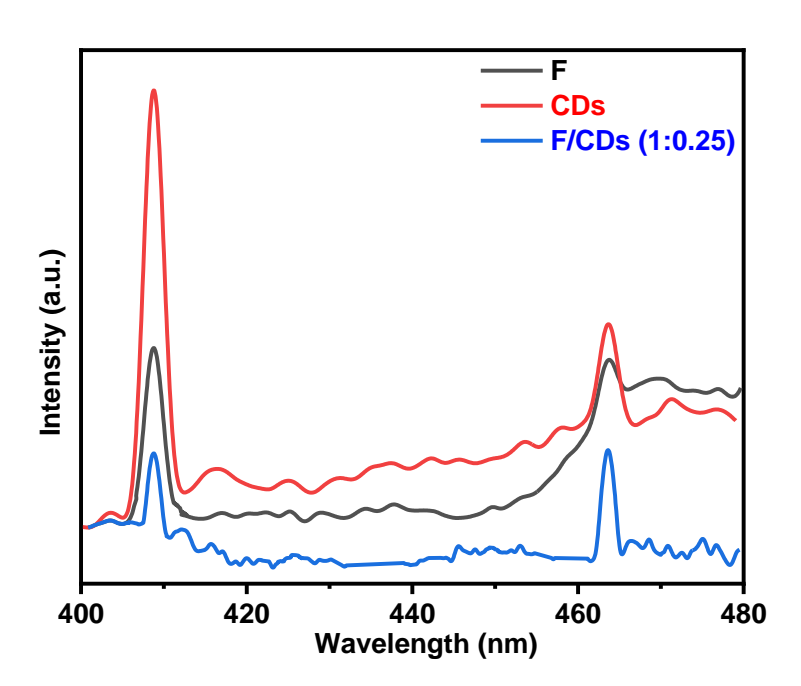


**Figure 7:** PL spectrum data for carbon dots,  $SrBaZn_{1.25}Mn_{0.75}Fe_{10.5}Si_{0.75}Ni_{0.75}O_{22}$ , and composite (CDs/SrBaZn<sub>1.25</sub>Mn<sub>0.75</sub>Fe<sub>10.5</sub>Si<sub>0.75</sub>Ni<sub>0.75</sub>O<sub>22</sub> with ratio 0.25/1.0).

# 3.4. Photocatalytic performance

To evaluate the photocatalytic properties of fabricated samples being exposed to visible light, rhodamine B (RhB) was adopted as a designated pollutant in this study. Control experiments were carried out to ensure that the photocatalyst and light were the main causes of the dye decomposition. Instead of using a catalyst, a 20 ppm dye solution was initially exposed to light. Secondly, 100 mL of dye solution was mixed with 0.01 g of catalyst while it was left in the dark for 30 minutes. There was no deterioration in any of the studies, though there was a tiny change in the dye solution's absorbance, which is possibly brought on by the surface adsorption of the photocatalyst. The inclusion of both photocatalysts and light resulted in dye deterioration. The following equation was used to compute the % dye degradation[62]:

$$\%\,Degradation = (1-C_t\,/C_o\,)\times 100$$

At time t, the dye concentration is denoted by  $C_t$ , and the concentration at time t = 0.0 is denoted by C<sub>o</sub>. The percent dye degradation employing different photocatalysts is shown in Figure 8a, such as carbon dots, substituted hexaferrite (SrBaZn<sub>1.25</sub>Mn<sub>0.75</sub>Fe<sub>10.5</sub>Si<sub>0.75</sub>Ni<sub>0.75</sub>O<sub>22</sub>), and their combination with various ratios (ferrites: carbon dots) i.e., 1:0.25, 1:0.5 and 1:0.75. Carbon dots and substituted hexaferrite photodegraded with 56 and 71 percent efficiency, respectively. The efficiency of composite materials with ratios 1:0.25, 1:0.5. and 1:0.75 of SrBaZn<sub>1.25</sub>Mn<sub>0.75</sub>Fe<sub>10.5</sub>Si<sub>0.75</sub>Ni<sub>0.75</sub>O<sub>22</sub>:CD was determined to be 94, 85, and 75 percent, respectively. Figures 8b–d illustrate how the absorbance varies over time for each of the materials produced in this work. The absorbance reduces over time, indicating that dye degradation is going to take place but the reduction in absorbance for the composite with a ratio of 1:0.25 is much higher as compared to other materials indicating its excellent efficiency [63]. When the carbon dot concentration exceeds from 1:0.25 ratio, the photocatalytic efficiency declines, which might be because the shielding effect prevents the ferrite from absorbing further light. The time dependence

degradation efficiency of RhB at various photocatalysts has been given in figure 8e. The degradation efficiency increase with time and attain the maximum value of 94% at time 80 minutes. The photocatalytic degradation efficiency of the present photocatalyst i.e. composite materials has been compared with similar type of composite materials in supplementary materials (table S1) showing its better efficiency with minimum time as compared to other related materials.

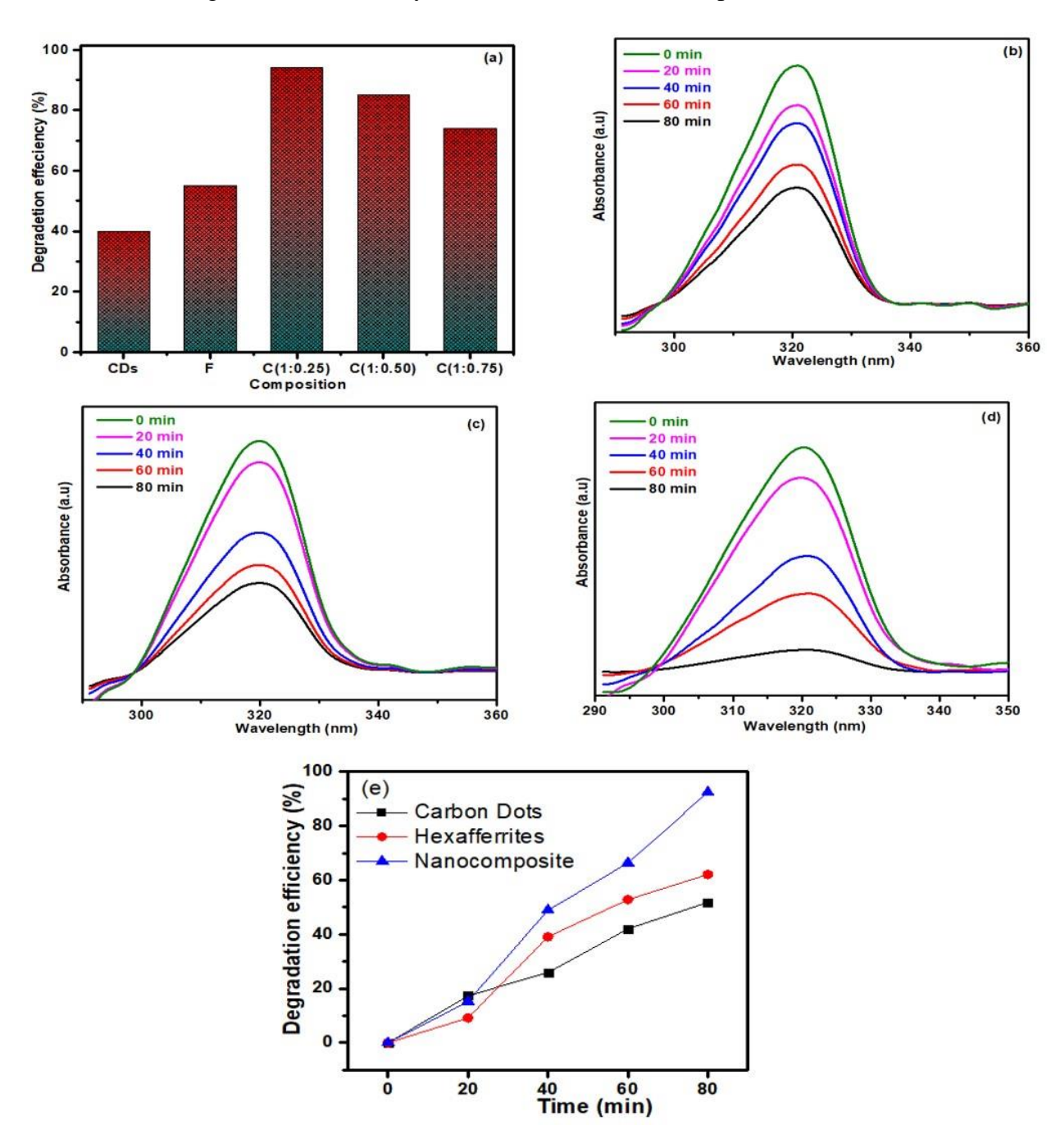


**Figure 8:** (a) RhB degradation in percentage using various photocatalysts, time-absorbance relationship for (b) carbon dots, (c)  $SrBaZn_{1.25}Mn_{0.75}Fe_{10.5}Si_{0.75}Ni_{0.75}O_{22}$ , (d) composite (CDs/SrBaZn<sub>1.25</sub>Mn<sub>0.75</sub>Fe<sub>10.5</sub>Si<sub>0.75</sub>Ni<sub>0.75</sub>O<sub>22</sub> with ratio 0.25/1.0) and (d) degradation efficiency with time.

#### 3.5. Reaction mechanism

By absorbing light, the photocatalysts create e<sup>-</sup>/h<sup>+</sup> pairs in conduction and valance band. The dye is degraded whenever these photoinduced charge species interact with water and oxygen to form reactive species [52]. Carbon dots and hexaferrite have lower efficiency due to electron-hole pair recombination and formation of less reactive species (•O<sup>-2</sup> and •OH). As a result, the photo-Fenton interaction may explain why ferrite materials outperform carbon dots. Electrons in the hexaferrite's conduction band react with ferric ions after light absorption, converting them to ferrous ions [53]. The Fenton reaction generates more •OH because there is a ferric/ferrous ion pair and the photodegradation efficiency of SrBaZn<sub>1.25</sub>Mn<sub>0.75</sub>Fe<sub>10.5</sub>Si<sub>0.75</sub>Ni<sub>0.75</sub>O<sub>22</sub> was much higher as compared to carbon dots.

The composite material with the maximum efficiency has a hexaferrite/carbon dots ratio of 1/0.25, which may be explained using PL analysis. The PL spectrum of the composite material has minimum peak intensity, showing that charge carrier recombination is less as compared to other materials which is responsible for the increased activity. These ideas can be applied to show why ferrite/CDs are more efficient than other photocatalysts. (a) By introducing their photon-excited particles into the conduction band of ferrites when exposed to visible light, CDs can act as an activator. (b) Through the  $\pi$ -  $\pi$ \* interaction, CDs can assist in the adsorption of organic contaminants, enhancing the effectiveness of the composite material. Additionally, by narrowing the energy gap between conduction and valence bands, the substantial conjugation positioned

inside the aromatic dye rings may help CDs carry out photocatalytic activity responses [64-67]. Figure 9a displays the outcomes of the tests for holes, •O-2, and •OH scavengers, which were carried out to learn more about the photocatalytic mechanism. When •OH scavenger (tertiary butanol), •O-2 scavenger (para-benzoquinone), and hole scavenger (EDTA-2Na) were used, the percentage degradation of rhodamine B dye decreased from 94% to 40.1%, 34.8%, and 59%, respectively. The •OH scavenger experiment demonstrated the highest loss in photocatalytic activity (from 94 to 34.8 percent), implying that •OH is the primary reactive component that destroys RhB, with holes and •O-2 playing a minor role.

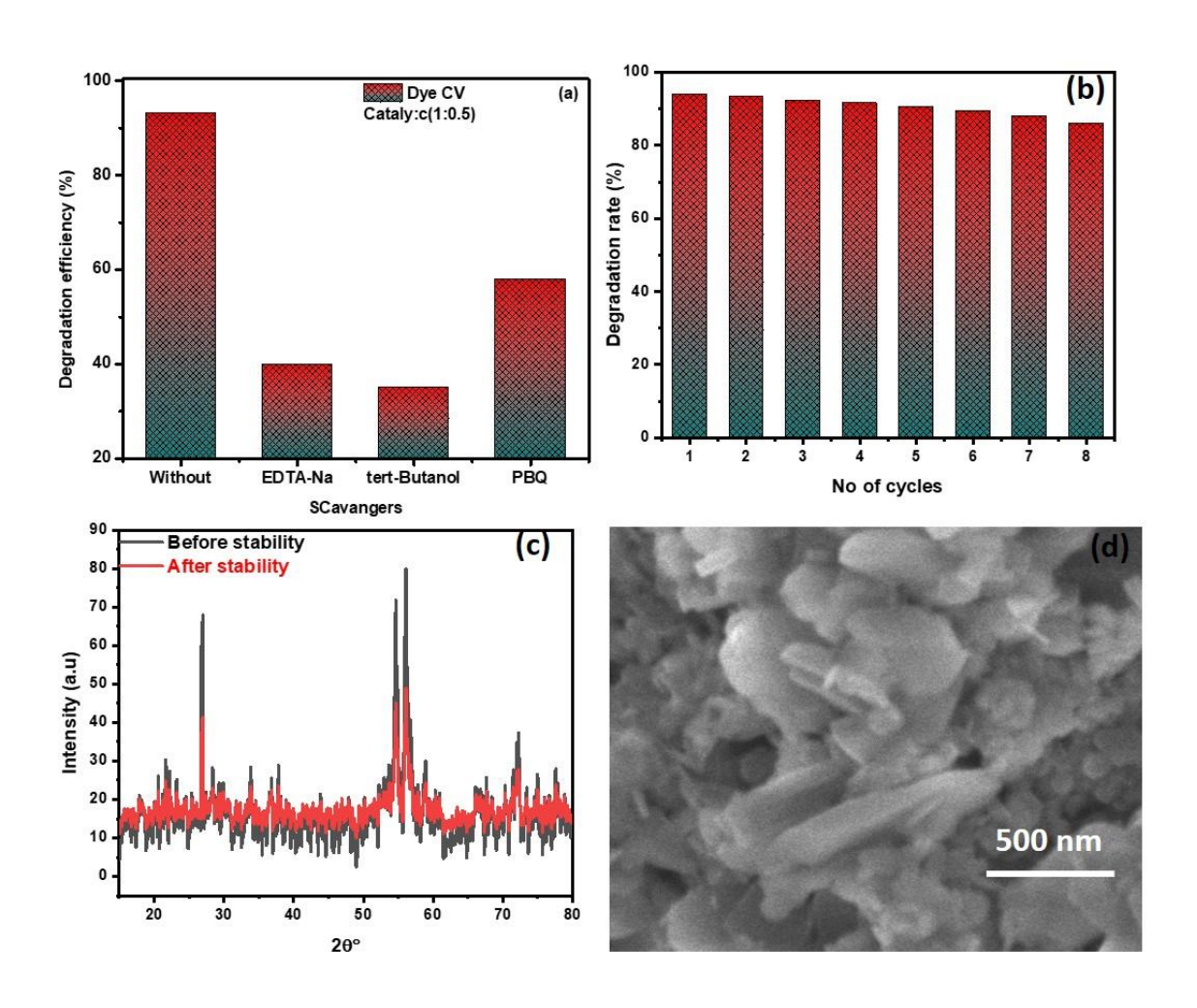


**Figure 9:** (a) Proportion of RhB degradation when scavengers are present, (b) Test for reusability and stability (c) before and after 8 consecutive runs XRD pattern and d) SEM micrograph of the composite after stability test.

Rhodamine B can be degraded photo-catalytically, as seen in Figure 10. In the first stage, the photocatalyst absorbs light and produces an electron/hole pair. After that, the electron combines with O<sub>2</sub> to produce the reactive species •O<sup>-2</sup>, which subsequently interacts with the proton to create the radicles •OH. The photo-Fenton reaction generated a huge number of •OH reactive species at the same time, resulting in holes. As a result, a large amount of •OH is created, which accounts for the composite material's increased efficiency.

The photocatalyst's durability and usage are equally as crucial as its effectiveness. In this work, the stability and reuse of the photocatalyst were also investigated. Using centrifugation, the (SrBaZn<sub>1.25</sub>Mn<sub>0.75</sub>Fe<sub>10.5</sub>Si<sub>0.75</sub>Ni<sub>0.75</sub>O<sub>22</sub>/CDs photocatalyst was enhanced and washed with deionized water three times before drying after being exposed to light for 80 minutes. Figure 9b shows the recycle periods of the (SrBaZn<sub>1.25</sub>Mn<sub>0.75</sub>Fe<sub>10.5</sub>Si<sub>0.75</sub>Ni<sub>0.75</sub>O<sub>22</sub>/CDs nanocomposite during the RhB photodegradation process. After five successive cycles, it was discovered that catalytic efficiency does not degrade significantly (figure 9b). Figure 9c shows the XRD analysis of the photocatalyst after five consecutive runs. The peaks in the XRD spectra were maintained at the same 2-theta levels before the photocatalytic cycles, demonstrating that the photocatalyst's crystal structure was unaltered, and a little reduction in the efficiency also indicates that the fabricated material in the present work can be effectively used for the photodegradation of industrially important dye RhB. Figure 9d represents the SEM micrographs of the nanocomposite to confirm the surface morphology, also indicating a little change in the shape of the nanocomposite. this little

change was also due to the adsorption of dye molecules on the surface of the fabricated material, which can cause the blockage of many active sites due to the long-term usability.

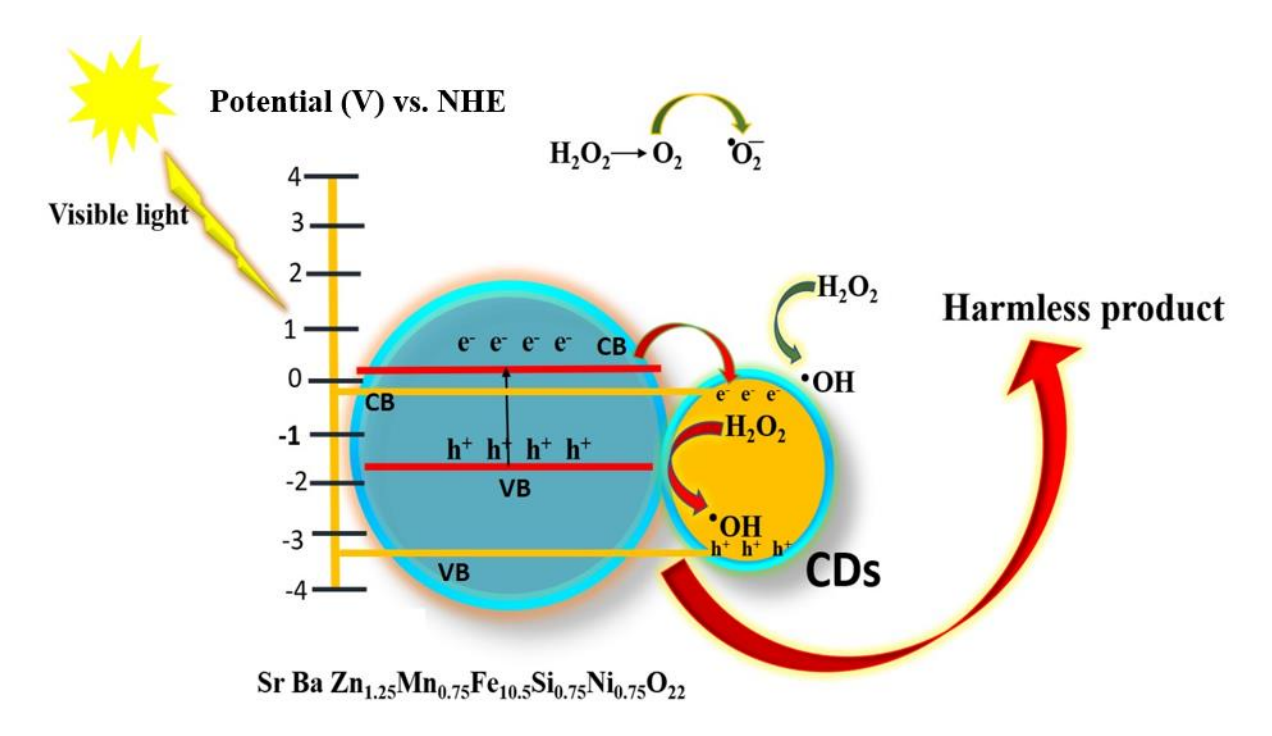


Figure 10: Diagram illustrating RhB's photodegradation process

#### **Conclusion**

Y-type hexaferrite substituted nanomaterials were perfectly synthesized using a traditional microemulsion technique. XRD validated the hexagonal phase, whereas BET, SEM, and UV/visible spectroscopy confirmed the shape, surface area, and band gap. Hysteresis loop measurements were used to determine the Ms, Mr, and Hc, and a two-point probe calculation was used to get the dc electrical resistivity. Coercivity decreases from 1.40 to 0.39 KOe, but saturation magnetization and remanence increase from 18.6 to 47.7 and 6.7 to 18.3 emu g<sup>-1</sup>, respectively.

Electrical resistance rises from 25.85×10<sup>6</sup> to 49.13×10<sup>6</sup> ohm cm as substituent concentration rises. Because of improvements in magnetic and electric properties, materials with the formula SrBaZn<sub>1.25</sub>Mn<sub>0.75</sub>Fe<sub>10.5</sub>Si<sub>0.75</sub>Ni<sub>0.75</sub>O<sub>22</sub> could be employed in recording media and microwave devices. Carbon dots with various ratios were added to SrBaZn<sub>1.25</sub>Mn<sub>0.75</sub>Fe<sub>10.5</sub>Si<sub>0.75</sub>Ni<sub>0.75</sub>O<sub>22</sub> and the sample with ratio 1:0.25 (SrBaZn<sub>1.25</sub>Mn<sub>0.75</sub>Fe<sub>10.5</sub>Si<sub>0.75</sub>Ni<sub>0.75</sub>O<sub>22</sub>: CDs) degrade the RhB up to 94 percent. To corroborate the photodegradation mechanism, trapping investigations were conducted, and the composite material showed to be highly robust while the trapping experiments suggested that •OH played a major role. This composite material has a high economic potential for degrading the Rhodamine B dye in aquatic conditions.

# Acknowledgment

K.F.F express appreciation to the Deanship of Scientific Research at King Khalid University Saudi Arabia for funding through the research groups program under grant number R.G.P. 2/279/44.

#### Reference

[1] G. Mittal, K.Y. Rhee, V. Mišković-Stanković, D. Hui, Reinforcements in multi-scale polymer composites: Processing, properties, and applications, Compos. Part B Eng. 138 (2018) 122–139. https://doi.org/10.1016/J.COMPOSITESB.2017.11.028.

- [2] Y. Cha, T. Kim, B. Seo, W. Choi, Combustion-driven synthesis route for bimetallic Ag–Bi nanoparticle-anchored carbon nanotube electrodes for high-performance supercapacitors, Carbon N. Y. 198 (2022) 11–21.
  https://doi.org/10.1016/J.CARBON.2022.07.003.
- [3] Y. Liu, Y. Wang, J. Ma, S. Li, H. Pan, C.W. Nan, Y.H. Lin, Controllable electrical, magnetoelectric and optical properties of BiFeO3 via domain engineering, Prog. Mater. Sci. 127 (2022) 100943. https://doi.org/10.1016/J.PMATSCI.2022.100943.
- [4] Z. Said, M.A. Sohail, R. Walvekar, C. Liu, Impact of sonication durations on thermophysical properties, contact angle and surface tension of f-MWCNTs nanofluid for heat transfer, J. Mol. Liq. 358 (2022) 119164. https://doi.org/10.1016/J.MOLLIQ.2022.119164.
- [5] C.I. Idumah, Influence of surfaces and interfaces on MXene and MXene hybrid polymeric nanoarchitectures, properties, and applications, J. Mater. Sci. 2022 5731. 57 (2022) 14579–14619. https://doi.org/10.1007/S10853-022-07526-9.
- [6] S.S. Ashok Kumar, S. Bashir, K. Ramesh, S. Ramesh, A review on graphene and its derivatives as the forerunner of the two-dimensional material family for the future, J. Mater. Sci. 57 (2022) 12236–12278. https://doi.org/10.1007/S10853-022-07346-X/FIGURES/23.
- [7] M. Abdullah, S. Hasany, M. Amir Qureshi, S. Hussain, Cost-Effective Synthesis of Cobalt Ferrite Nanoparticles by Sol-Gel Technique, Mater. Sci. Forum. 1067 (2022) 213–219. https://doi.org/10.4028/P-JDLQ11.
- [8] H.G. Abd-Elbaky, M. Rasly, R.G. Deghadi, G.G. Mohamed, M.M. Rashad, Strong-base free synthesis enhancing the structural, magnetic and optical properties of Mn/Co and

- Zn/Co substituted cobalt ferrites, J. Mater. Res. Technol. 20 (2022) 905–915. https://doi.org/10.1016/J.JMRT.2022.07.106.
- [9] S.I. Ahmad, Nano cobalt ferrites: Doping, Structural, Low-temperature, and room temperature magnetic and dielectric properties – A comprehensive review, J. Magn. Magn. Mater. 562 (2022) 169840. https://doi.org/10.1016/J.JMMM.2022.169840.
- [10] R.M. Almeida, W. Paraguassu, D.S. Pires, R.R. Corrêa, C.W. de Araujo Paschoal, Impedance spectroscopy analysis of BaFe12O19 M-type hexaferrite obtained by ceramic method, Ceram. Int. 35 (2009) 2443–2447. https://doi.org/10.1016/J.CERAMINT.2009.02.020.
- [11] R. Tajima, K. Kamishima, K. Kakizaki, N. Hiratsuka, A. Fujimori, M. Sakai, K. Watanabe, Synthesis of a new U-type hexaferrite Ba4Cu2Fe36O60, Trans. Mater. Res. Soc. Japan. 38 (2013) 451–454. https://doi.org/10.14723/TMRSJ.38.451.
- [12] B.X. Gu, Magnetic properties of X- type Ba2Me2Fe28O46 (Me=Fe, Co, and Mn) hexagonal ferrites, J. Appl. Phys. 71 (1998) 5103. https://doi.org/10.1063/1.350613.
- [13] N. Amin, R. Bilal, G. Mustafa, A. Aslam, M.S. Hasan, K. Hussain, M. Tabassum, M. Fatima, Z.E. Khan, A. Naseem, M. Akhtar, M. Gulzar, I. Younas, S. Amin, S. Shakeel, , Qurat-Ul-Ain, M.I. Arshad, IMPACTS OF SUBSTITUTING Ni 2+ IONS ON STRUCTURAL AND ELECTRICAL PROPERTIES OF W-TYPE BARIUM BASED HEXAFERRITES, Dig. J. Nanomater. Biostructures. 14 (n.d.) 501–507.
- [14] Y.B. Lee, J.T. Lim, C.S. Kim, Investigation of Ba2Me2Fe12O22 (M = Co, Zn) hexaferrite based on external magnetic field Mössbauer spectroscopy, J. Korean Phys. Soc. 2014 659. 65 (2014) 1419–1422. https://doi.org/10.3938/JKPS.65.1419.
- [15] E.S. Ramakrishnan, K.D. Cornett, G. Srinivasan, Synthesis of-type hexagonal ferrite films

- by rf magnetron sputtering techniques (abstract) ARTICLES YOU MAY BE INTERESTED IN A new model for dark solitons in magnetic films, J. Appl. Phys. 81 (1997) 5159. https://doi.org/10.1063/1.365156.
- [16] N. Morin-Crini, E. Lichtfouse, G. Torri, G. Crini, Applications of chitosan in food, pharmaceuticals, medicine, cosmetics, agriculture, textiles, pulp and paper, biotechnology, and environmental chemistry, Environ. Chem. Lett. 2019 174. 17 (2019) 1667–1692. https://doi.org/10.1007/S10311-019-00904-X.
- [17] D. Lithner, A. Larsson, G. Dave, Environmental and health hazard ranking and assessment of plastic polymers based on chemical composition, Sci. Total Environ. 409 (2011) 3309–3324. https://doi.org/10.1016/J.SCITOTENV.2011.04.038.
- [18] I.A. Bello, N.A. Kabbashi, M.Z. Alam, M.F. Alkhatib, F.N. Murad, I.Y. Qudsieh, CHALLENGES IN TEXTILE WASTEWATER AND CURRENT PALLIATIVE METHODS: AN OVERVIEW, IIUM Eng. J. 18 (2017) 71–78. https://doi.org/10.31436/IIUMEJ.V18I2.742.
- [19] D. Bhatia, N.R. Sharma, J. Singh, R.S. Kanwar, Biological methods for textile dye removal from wastewater: A review, Https://Doi.Org/10.1080/10643389.2017.1393263.
   47 (2017) 1836–1876. https://doi.org/10.1080/10643389.2017.1393263.
- [20] B. Padhi, Pollution due to synthetic dyes toxicity & carcinogenicity studies and remediation, Int. J. Environ. Sci. 3 (2012) 940–955. https://doi.org/10.6088/IJES.2012030133002.
- [21] Q.Y. Yue, B.Y. Gao, Y. Wang, H. Zhang, X. Sun, S.G. Wang, R.R. Gu, Synthesis of polyamine flocculants and their potential use in treating dye wastewater, J. Hazard. Mater. 152 (2008) 221–227. https://doi.org/10.1016/J.JHAZMAT.2007.06.089.

- [22] K.B. Tan, M. Vakili, B.A. Horri, P.E. Poh, A.Z. Abdullah, B. Salamatinia, Adsorption of dyes by nanomaterials: Recent developments and adsorption mechanisms, Sep. Purif. Technol. 150 (2015) 229–242. https://doi.org/10.1016/J.SEPPUR.2015.07.009.
- [23] L. Lucarelli, V. Nadtochenko, J. Kiwi, Environmental photochemistry: quantitative adsorption and FTIR studies during the TiO2-photocatalyzed degradation of Orange II, Langmuir. 16 (2000) 1102–1108.
  https://doi.org/10.1021/LA990272J/ASSET/IMAGES/LARGE/LA990272JF00008.JPEG.
- [24] T. Zahra, K.S. Ahmad, C. Zequine, R.K. Gupta, A.G. Thomas, M.A. Malik, S.B. Jaffri, D. Ali, Electro-catalyst [ZrO2/ZnO/PdO]-NPs green functionalization: Fabrication, characterization and water splitting potential assessment, Int. J. Hydrogen Energy. 46 (2021) 19347–19362. https://doi.org/10.1016/J.IJHYDENE.2021.03.094.
- [25] S. Sadri Moghaddam, M.R. Alavi Moghaddam, M. Arami, Coagulation/flocculation process for dye removal using sludge from water treatment plant: Optimization through response surface methodology, J. Hazard. Mater. 175 (2010) 651–657. https://doi.org/10.1016/J.JHAZMAT.2009.10.058.
- [26] R. Vinayagam, R. Selvaraj, P. Arivalagan, T. Varadavenkatesan, Synthesis, characterization and photocatalytic dye degradation capability of Calliandra haematocephala-mediated zinc oxide nanoflowers, J. Photochem. Photobiol. B Biol. 203 (2020) 111760. https://doi.org/10.1016/J.JPHOTOBIOL.2019.111760.
- [27] A. Akbari, Z. Sabouri, H.A. Hosseini, A. Hashemzadeh, M. Khatami, M. Darroudi, Effect of nickel oxide nanoparticles as a photocatalyst in dyes degradation and evaluation of effective parameters in their removal from aqueous environments, Inorg. Chem. Commun. 115 (2020) 107867. https://doi.org/10.1016/J.INOCHE.2020.107867.

- [28] L. Gnanasekaran, R. Hemamalini, R. Saravanan, K. Ravichandran, F. Gracia, S. Agarwal, V.K. Gupta, Synthesis and characterization of metal oxides (CeO2, CuO, NiO, Mn3O4, SnO2 and ZnO) nanoparticles as photo catalysts for degradation of textile dyes, J. Photochem. Photobiol. B Biol. 173 (2017) 43–49. https://doi.org/10.1016/J.JPHOTOBIOL.2017.05.027.
- [29] R. Suresh, K. Giribabu, R. Manigandan, R. V. Mangalaraja, J.Y. Solorza, A. Stephen, V. Narayanan, Synthesis of Co2+-doped Fe2O3 photocatalyst for degradation of pararosaniline dye, Solid State Sci. 68 (2017) 39–46.
  https://doi.org/10.1016/J.SOLIDSTATESCIENCES.2017.04.005.
- [30] X. Zhao, Y. Xu, X. Wang, Q. Liang, M. Zhou, S. Xu, Z. Li, Construction and enhanced efficiency of Z-scheme-based ZnCdS/Bi2WO6 composites for visible-light-driven photocatalytic dye degradation, J. Phys. Chem. Solids. 154 (2021) 110075. https://doi.org/10.1016/J.JPCS.2021.110075.
- [31] A. Taufik, R. Saleh, Combination of ternary Fe3O4/TiO2/CuO nanocomposites and nanographene platelets: High performance photo and sonocatalysis, AIP Conf. Proc. 1788 (2017) 030037. https://doi.org/10.1063/1.4968290.
- [32] M.D. Hossain, STRUCTURAL AND MAGNETIC CHARACTERIZATION OF SPINEL FERRITES WITH HIGH MAGNETIZATION, (2015).
- [33] S.A. Mathews, D.R. Babu, Analysis of the role of M-type hexaferrite-based materials in electromagnetic interference shielding, Curr. Appl. Phys. 29 (2021) 39–53. https://doi.org/10.1016/J.CAP.2021.06.001.
- [34] X. Li, Y. Fu, S. Zhao, J.F. Xiao, M. Lan, B. Wang, K. Zhang, X. Song, L. Zeng, Metal ions-doped carbon dots: Synthesis, properties, and applications, Chem. Eng. J. 430 (2022)

- 133101. https://doi.org/10.1016/J.CEJ.2021.133101.
- [35] Zhou, L., Yang, T., Fang, Z., Zhou, J., Zheng, Y., Guo, C., Zhu, L., Wang, E., Hou, X., Chou, K.C. and Wang, Z.L., 2022. Boosting of water splitting using the chemical energy simultaneously harvested from light, kinetic energy and electrical energy using N doped 4H-SiC nanohole arrays. Nano Energy, 104, p.107876. https://doi.org/10.1016/j.nanoen.2022.107876
- [36] Liu, Shuang, Tao Yang, Enhui Wang, Hailong Wang, Zhentao Du, Sheng Cao, Qiaobao Zhang, Kuo-Chih Chou, and Xinmei Hou. Ultra-stable and bifunctional free-standing SiC photoelectrocatalyst for water remediation. J. Clean. Prod. 396 (2023): 136484. https://doi.org/10.1016/j.jclepro.2023.136484.
- [37] Zhong, Shuiping, Huanlin Zhu, Lei Yang, Xiaopeng Chi, Wen Tan, and Wei Weng.

  Activating bulk nickel foam for the electrochemical oxidization of ethanol by anchoring

  MnO 2@ Au nanorods. J. Mater. Chem. A. 11, no. 15 (2023): 8101-8109.

  https://doi.org/10.1039/D3TA00367A
- [38] G. Lui, J.Y. Liao, A. Duan, Z. Zhang, M. Fowler, A. Yu, Graphene-wrapped hierarchical TiO2 nanoflower composites with enhanced photocatalytic performance, J. Mater. Chem. A. 1 (2013) 12255–12262. https://doi.org/10.1039/C3TA12329D.
- [39] T. Dippong, E.A. Levei, C. Tanaselia, M. Gabor, M. Nasui, L. Barbu Tudoran, G. Borodi, Magnetic properties evolution of the CoxFe3-xO4/SiO2 system due to advanced thermal treatment at 700 °C and 1000 °C, J. Magn. Magn. Mater. 410 (2016) 47–54. https://doi.org/10.1016/J.JMMM.2016.03.020.
- [40] T. DIppong, E.A. Levei, O. Cadar, Preparation of CoFe2O4/SiO2 Nanocomposites at Low Temperatures Using Short Chain Diols, J. Chem. 2017 (2017).

- https://doi.org/10.1155/2017/7943164.
- [41] T. Dippong, E.A. Levei, G. Borodi, F. Goga, L. Barbu Tudoran, Influence of Co/Fe ratio on the oxide phases in nanoparticles of CoxFe3-xO4, J. Therm. Anal. Calorim. 119 (2015) 1001–1009. https://doi.org/10.1007/S10973-014-4280-7/FIGURES/17.
- [42] M.J. Iqbal, M.N. Ashiq, P. Hernandez-Gomez, J.M. Munoz, Synthesis, physical, magnetic and electrical properties of Al–Ga substituted co-precipitated nanocrystalline strontium hexaferrite, J. Magn. Magn. Mater. 320 (2008) 881–886. https://doi.org/10.1016/J.JMMM.2007.09.005.
- [43] V. Shelke, S. Khatarkar, R. Rawat, R.K. Singh, Open atmosphere synthesis and wide range colossal magnetoresistance in La0.7Sr0.3−xHgxMnO3 (0≤x≤0.2) system, Solid State Commun. 135 (2005) 208–213. https://doi.org/10.1016/J.SSC.2005.02.031.
- [44] C.M.B. Henderson, Í.L. de Oliveira, Substitution of 'small' divalent cations (e.g. Mg) for Si and Al in the nepheline tetrahedral framework: 1. Calculation of atomic formulae and stoichiometry parameters, Mineral. Mag. 86 (2022) 243–253. https://doi.org/10.1180/MGM.2022.24.
- [45] M.J. Iqbal, S. Farooq, Extraordinary role of Ce–Ni elements on the electrical and magnetic properties of Sr–Ba M-type hexaferrites, Mater. Res. Bull. 44 (2009) 2050–2055. https://doi.org/10.1016/J.MATERRESBULL.2009.07.015.
- [46] J. Hu, X. Liu, X. Kan, S. Feng, C. Liu, Y. Yang, Q. Lv, Synthesis, analysis and characterization of Co substituted NiZnTi spinel ferrite, J. Alloys Compd. 828 (2020) 154181. https://doi.org/10.1016/J.JALLCOM.2020.154181.
- [47] Y. Xin, J.G. Liu, Y. Zhou, W. Liu, J. Gao, Y. Xie, Y. Yin, Z. Zou, Preparation and characterization of Pt supported on graphene with enhanced electrocatalytic activity in

- fuel cell, J. Power Sources. 196 (2011) 1012–1018. https://doi.org/10.1016/J.JPOWSOUR.2010.08.051.
- [48] M. Ogura, K. Itabashi, J. Dedecek, T. Onkawa, Y. Shimada, K. Kawakami, K. Onodera, S. Nakamura, T. Okubo, Stabilization of bare divalent Fe(II) cations in Al-rich beta zeolites for superior NO adsorption, J. Catal. 315 (2014) 1–5.
  https://doi.org/10.1016/J.JCAT.2014.04.001.
- [49] I. Jendoubi, R. Ben Smail, M. Maczka, M.F. Zid, Optical and electrical properties of the yavapaiite-like molybdate NaAl(MoO4)2, Ionics (Kiel). 24 (2018) 3515–3533. https://doi.org/10.1007/S11581-018-2490-X/FIGURES/19.
- [50] S.H. Mahmood, M.D. Zaqsaw, O.E. Mohsen, A. Awadallah, I. Bsoul, M. Awawdeh, Q.I. Mohaidat, Modification of the Magnetic Properties of Co2Y Hexaferrites by Divalent and Trivalent Metal Substitutions, Solid State Phenom. 241 (2016) 93–125. https://doi.org/10.4028/WWW.SCIENTIFIC.NET/SSP.241.93.
- [51] M. Ahmad, I. Ali, R. Grössinger, M. Kriegisch, F. Kubel, M.U. Rana, Effects of divalent ions substitution on the microstructure, magnetic and electromagnetic parameters of Co2W hexagonal ferrites synthesized by sol–gel method, J. Alloys Compd. 579 (2013) 57–64. https://doi.org/10.1016/J.JALLCOM.2013.04.115.
- [52] V. Uvarov, I. Popov, Metrological characterization of X-ray diffraction methods for determination of crystallite size in nano-scale materials, Mater. Charact. 58 (2007) 883– 891. https://doi.org/10.1016/J.MATCHAR.2006.09.002.
- [53] N. Yasmin, S. Yasmin, M. Zahid, S.F. Gillani, M.U. Islam, M. Altaf, H.M. Khan, M. Safdar, M. Mirza, Impact of Ho-Ni substitution on structural, morphological and dielectrical characteristics of BaFe12O19 M-type hexagonal ferrite, Phys. B Condens.

- Matter. 581 (2020) 411950. https://doi.org/10.1016/J.PHYSB.2019.411950.
- [54] A. Tkach, T.M. Correia, A. Almeida, J. Agostinho Moreira, M.R. Chaves, O. Okhay, P.M. Vilarinho, I. Gregora, J. Petzelt, Role of trivalent Sr substituents and Sr vacancies in tetragonal and polar states of SrTiO3, Acta Mater. 59 (2011) 5388–5397. https://doi.org/10.1016/J.ACTAMAT.2011.05.011.
- [55] C. Nordhei, A.L. Ramstad, D.G. Nicholson, Nanophase cobalt, nickel and zinc ferrites: synchrotron XAS study on the crystallite size dependence of metal distribution, Phys. Chem. Chem. Phys. 10 (2008) 1053–1066. https://doi.org/10.1039/B711918F.
- [56] M.M. Kothawale, R.B. Tangsali, G.K. Naik, J.S. Budkuley, Characterization and magnetic properties of nanoparticle Ni 1-xZn xFe 2O 4 ferrites prepared using microwave assisted combustion method, J. Supercond. Nov. Magn. 25 (2012) 1907–1911. https://doi.org/10.1007/S10948-012-1510-8/FIGURES/6.
- [57] S.M. Abbas, R. Chatterjee, A.K. Dixit, A.V.R. Kumar, T.C. Goel, Electromagnetic and microwave absorption properties of (Co2+–Si4+) substituted barium hexaferrites and its polymer composite, J. Appl. Phys. 101 (2007) 074105. https://doi.org/10.1063/1.2716379.
- [58] T. Dippong, E.A. Levei, I.G. Deac, I. Petean, O. Cadar, Dependence of Structural, Morphological and Magnetic Properties of Manganese Ferrite on Ni-Mn Substitution, Int. J. Mol. Sci. 2022, Vol. 23, Page 3097. 23 (2022) 3097. https://doi.org/10.3390/IJMS23063097.
- [59] T. Dippong, E.A. Levei, O. Cadar, Investigation of Structural, Morphological and Magnetic Properties of MFe2O4 (M = Co, Ni, Zn, Cu, Mn) Obtained by Thermal Decomposition, Int. J. Mol. Sci. 2022, Vol. 23, Page 8483. 23 (2022) 8483. https://doi.org/10.3390/IJMS23158483.

- [60] T. Dippong, I.G. Deac, O. Cadar, E.A. Levei, Effect of Silica Embedding on the Structure, Morphology and Magnetic Behavior of (Zn0.6Mn0.4Fe2O4)δ/(SiO2)(100-δ) Nanoparticles, Nanomater. 2021, Vol. 11, Page 2232. 11 (2021) 2232. https://doi.org/10.3390/NANO11092232.
- [61] M. Abdullah, · Peter John, · Muhammad, N. Ashiq, · Sumaira Manzoor, I. Ghori, · Mehar, U. Nisa, · Abdul, G. Abid, · Kashif, Y. Butt, S. Ahmed, Development of CuO/CuS/MnO2 ternary nanocomposite for visible light-induced photocatalytic degradation of methylene blue, Nanotechnol. Environ. Eng. 2022. 1 (2022) 1–11. https://doi.org/10.1007/S41204-022-00266-W.
- [62] M. Abdullah, P. John, Z. Ahmad, M.N. Ashiq, S. Manzoor, M.I. Ghori, M.U. Nisa, A.G. Abid, K.Y. Butt, S. Ahmed, Visible-light-driven ZnO/ZnS/MnO2 ternary nanocomposite catalyst: synthesis, characterization and photocatalytic degradation of methylene blue, Appl. Nanosci. 11 (2021) 2361–2370. https://doi.org/10.1007/S13204-021-02008-X/TABLES/1.
- [63] N. Greenham, X. Peng, A. Alivisatos, Charge separation and transport in conjugated-polymer/semiconductor-nanocrystal composites studied by photoluminescence quenching and photoconductivity, Phys. Rev. B. 54 (1996) 17628.
  https://doi.org/10.1103/PhysRevB.54.17628.
- [64] X. Li, Y. Wang, H. Sun, H. Zeng, X.M. Li, B. Zeng, Y. Wang, D. Sun, Amino-Mediated Anchoring Perovskite Quantum Dots for Stable and Low-Threshold Random Lasing, Adv. Mater. 29 (2017) 1701185. https://doi.org/10.1002/ADMA.201701185.
- [65] A. Haghighatzadeh, Comparative analysis on optical and photocatalytic properties of chlorophyll/curcumin-sensitized TiO 2 nanoparticles for phenol degradation, Bull. Mater.

- Sci. 43 (2020) 1–15. https://doi.org/10.1007/S12034-019-2016-9/FIGURES/9.
- [66] F. Wang, K. Zhang, Reduced graphene oxide—TiO<sub>2</sub> nanocomposite with high photocatalystic activity for the degradation of rhodamine B, J. Mol. Catal. A Chem. 345 (2011) 101–107. https://doi.org/10.1016/J.MOLCATA.2011.05.026.
- [67] K. Khan, Z. Batool, S. Manzoor, D. Ahmad, S. Aman, D. Alhashmialameer, H.H. Abd El-Gawad, T.A. Taha, M.N. Ashiq, Fabrication of substituted Y-type hexaferrites/carbon dots composites for recording media and photodegradation of dye, Ceram. Int. 48 (2022) 27550–27559. https://doi.org/10.1016/J.CERAMINT.2022.06.048.

#### **Declaration Statement**

The authors declare that they have no known competing financial interests or personal relationships that could have appeared to influence the work reported in this paper.

The manuscript has not been published previously, and is not under consideration for publication elsewhere. It is also stated that the work is original. The publication is approved by all authors and tacitly or explicitly by the responsible authorities where the work was carried out. If accepted, it will not be published elsewhere in the same form, in English or in any other language, including electronically without the written consent of the copyright-holder. In addition, the authors have no conflicts of interest to declare.